Antiferromagnetic Chern insulator in centrosymmetric systems

Morad Ebrahimkhas,[1,2,*] Götz S. Uhrig,[3,†] Walter Hofstetter,[1,‡] and Mohsen Hafez-Torbati[3,§]
[1]*Goethe-Universität Frankfurt, Institut für Theoretische Physik, Frankfurt, Germany*
[2]*Department of Physics, Mahabad Branch, Islamic Azad University, Mahabad, Iran*
[3]*Condensed Matter Theory, Department of Physics, TU Dortmund University, 44221 Dortmund, Germany*

(Received 12 September 2022; accepted 27 October 2022; published 4 November 2022)

An antiferromagnetic Chern insulator (AFCI) can exist if the effect of the time-reversal transformation on the electronic state cannot be compensated by a space-group operation. The AFCI state with collinear magnetic order is already realized in noncentrosymmetric honeycomb structures through the Kane-Mele-Hubbard model. In this paper, we demonstrate the existence of the collinear AFCI in a square-lattice model which preserves the inversion symmetry. Our study relies on the time-reversal-invariant Harper-Hofstadter-Hubbard model extended by a next-nearest-neighbor hopping term including spin-orbit coupling and a checkerboard potential. We show that an easy z-axis AFCI appears between the band insulator at weak and the easy xy-plane AF Mott insulator at strong Hubbard repulsion provided the checkerboard potential is large enough. The close similarity between our results and the results obtained for the noncentrosymmetric Kane-Mele-Hubbard model suggests the AFCI as a generic consequence of spin-orbit coupling and strong electronic correlation which exists beyond a specific model or lattice structure. An AFCI with the electronic and the magnetic properties originating from the same strongly interacting electrons is a promising candidate for a strong magnetic blueshift of the charge gap below the Néel temperature and for realizing the quantum anomalous Hall effect at higher temperatures so that applications for data processing become possible.

DOI: 10.1103/PhysRevB.106.205107

I. INTRODUCTION

The precise quantization of the Hall conductance in a two-dimensional (2D) electron gas system subject to a strong perpendicular magnetic field at low temperatures led to the discovery of the quantum Hall state. A quantum Hall state is characterized by a nonzero topological invariant $\mathcal{C}$ known as Chern number. The state shows insulating behavior in the bulk and metallic behavior at the edges. The gapless edge states are chiral, i.e., electrons at each edge can only propagate in a single direction, either clockwise or anticlockwise. It is determined solely by the direction of the applied magnetic field. This prevents backscattering and permits dissipationless charge transport at the edges [1,2].

While a strong external magnetic field was essential in the discovery of the quantum Hall state, the Haldane model [3] provided a theoretical demonstration that a quantum Hall state can be achieved even without a net magnetic flux through the system. The only necessary condition is breaking of the time-reversal symmetry. This suggested that the quantum Hall state can be an intrinsic feature of a material rather than an effect induced by an external magnetic field. Such a state is known as the quantum anomalous Hall state or Chern insulator (CI). From a practical point of view, the CI is highly favorable for establishing dissipationless charge transport since it requires no strong external magnetic field [4,5].

The extension of the Haldane model to a spinful time-reversal-invariant (TRI) model led to the prediction of the quantum spin Hall insulator (QSHI) [6]. In a QSHI [6,7] the Chern number for up and down spins is opposite due to the time-reversal symmetry and the total Chern number $\mathcal{C} = \mathcal{C}_\uparrow + \mathcal{C}_\downarrow$ vanishes. The QSHI is characterized by a $\mathbb{Z}_2$ topological invariant $\nu = (\mathcal{C}_\uparrow - \mathcal{C}_\downarrow)/2$ modulo 2. There are gapless edge states which have opposite chirality for opposite spins. The QSHI remains robust against spin-mixing Rashba-type spin-orbit couplings due to the Kramers degeneracy [1,2]. The theoretical prediction of the QSHI in quantum wells [8] was soon followed by an experimental verification [9]. The generalization of the QSHI to three dimensions led to the theoretical prediction and the experimental observation of three-dimensional (3D) TRI topological insulators. While the quantum Hall state is a result of strong external magnetic fields, the TRI topological insulators stem from strong spin-orbit coupling [1,2].

Despite the important role that the Haldane model played in the discovery of the TRI topological insulators, the realization of the CI, for which the Haldane model was originally proposed, still remained elusive. This originated from the fact that the Haldane model was introduced more for theoretical aims rather than to be materialized. We would like to point out that the Haldane model is simulated in optical lattices by creating artificial gauge fields for neutral atoms [10].

The realization of the CI in a crystalline material requires two main ingredients: a strong spin-orbit coupling and a spontaneous breaking of the time-reversal symmetry via spontaneous magnetization [4,5]. An effective strategy to reach these conditions is by doping a topological insulator with

*ebrahimkhas@itp.uni-frankfurt.de
†goetz.uhrig@tu-dortmund.de
‡hofstett@physik.uni-frankfurt.de
§mohsen.hafez@tu-dortmund.de

magnetic impurities. A topological insulator has the prerequisite of strong spin-orbit coupling and magnetic impurities introduce magnetism into the system. A CI has been realized by doping thin films of the topological insulator $(Bi,Sb)_2Te_3$ with the transition-metal element Cr [11] following a theoretical proposal [12]. A precise quantization of the Hall resistance is observed at the temperature 30 mK at zero magnetic field [11]. Improving the sample quality has allowed the realization of the CI at the higher temperature 300 mK [13]. The fact that the CI is realized at a temperature two orders of magnitude smaller than the Curie temperature of the material, 30 K, is attributed to the strong inhomogeneity induced into the system by magnetic doping [14]. The temperature is raised to 2 K using a magnetic modulation doping technique [14].

There has been a large interest in recent years in finding topological insulators with intrinsic magnetic order [15] which would allow the elimination of the detrimental effect of disorder and an observation of the CI at higher temperature. The efforts have led to the identification of several intrinsic magnetic topological insulators, among them, $MnBi_2Te_4$ has attracted the most attention [16–25]. However, these systems have a very weak coupling between the magnetism and the electronic surface states. A magnetically induced gap in the surface states which is essential to realize the CI at high temperatures is either missing or is extremely small [22–25]. The CI is observed on thin films of $MnBi_2Te_4$ with an odd number of layers but still limited to the small temperature of 1.4 K [26]. This encourages further research to find the CI in a new class of systems.

The current realization of the CI is tied to ferromagnetic ordering [4,5]. One notes that although $MnBi_2Te_4$ is an antiferromagnet (A-type) the realization of the CI in its thin films [26] is due to the top and the bottom ferromagnetic layers. In addition, the magnetic and the electronic properties originate from electrons in different orbitals. While strongly correlated electrons in a partially filled $3d$ or $4f$ orbital are responsible for the magnetic ordering, the noninteracting electrons in $6p$ and $5p$ orbitals mainly govern the electronic properties [24]. The electronic bands are only indirectly affected by the magnetic ordering via an AF Kondo interaction [27].

Antiferromagnets are a large class of materials with unique features. They create no stray field, they are robust against disturbing magnetic fields, and they have ultrafast spin dynamics in contrast to ferromagnets. These are the reasons behind the recent surge of interest for developing a spintronics technology based on antiferromagnets [28]. In addition, there is experimental and theoretical evidence of antiferromagnets displaying a strong coupling between the magnetic and the electronic properties [29–35]. This is especially the case if the electrons defining the charge gap are the ones responsible for the magnetic ordering, i.e., strongly correlated [34,35]. There is a noticeable shift of the charge gap towards higher energies upon developing the AF order below the Néel temperature [34,35]. These features make identifying strongly correlated systems which can host antiferromagnetic CI (AFCI) states of particular interest. We emphasize that the AFCI discussed in this paper originates from the *spontaneous* time-reversal symmetry breaking which is distinct from the AF quantum Hall insulator [36,37] in which the time-reversal symmetry is explicitly broken.

A ferromagnetic ordering makes a clear distinction between up and down spins. This allows one spin component to be in a trivial state with $\mathcal{C}_\sigma = 0$ and the other spin component to be in a quantum Hall state with $\mathcal{C}_{\bar{\sigma}} \neq 0$, resulting in a CI with $\mathcal{C} = \mathcal{C}_\uparrow + \mathcal{C}_\downarrow \neq 0$. In contrast, such a distinction is not obvious in an antiferromagnet. This raises the question if there can exist an AFCI state. An AFCI can indeed exist if the effect of the time-reversal transformation on the electronic state cannot be compensated by a space-group operation. The absence of such an antiunitary symmetry is necessary for finding a nonzero Chern number [38,39]. The AFCI has already been identified in the Kane-Mele-Hubbard model which lacks inversion symmetry using a mean-field theory approximation [39] and is also suggested for $NiRuCl_6$ based on the density-functional theory analysis [40].

In this paper, we consider a minimal TRI extension of the Harper-Hofstadter model [41–43] which allows us to realize both the QSHI and the trivial band insulator (BI) at half-filling. In addition to the nearest-neighbor (NN) hopping t the Hamiltonian involves a next-nearest-neighbor (NNN) hopping t' and a checkerboard potential Δ. The combination of time-reversal symmetry and inversion symmetry with respect to a lattice site leads to spin-degenerate energy bands. We address the effect of the Hubbard interaction U favoring a Néel AF Mott insulator on the system employing the dynamical mean-field theory (DMFT) method [44]. We determine the phase diagram of the model in the U-Δ plane for a fixed value of t' and show that for $(U \approx 2\Delta) \gg t$ an easy z-axis AFCI appears, separating the BI at small and the easy xy-plane AF Mott insulator at large values of U.

The similarity between our results and the results obtained for the noncentrosymmetric Kane-Mele-Hubbard model [39] suggests the AFCI as a generic phase in strongly correlated systems with spin-orbit coupling, which exists beyond a specific model or lattice structure. We discuss the stabilization of the AFCI based on vanishing of spin and charge gaps and emphasize that the necessary condition to realize the AFCI is the absence of a space-group operation to compensate the effect of the time-reversal transformation on the electronic state.

The paper is organized as follows. In the next section we introduce the extended TRI Harper-Hofstadter-Hubbard (HHH) model and present its phase diagram. Section III is devoted to the technical aspects. In Sec. IV we discuss the results obtained for small to intermediate values of the checkerboard potential Δ. We unfold the emergence of the AFCI for large values of Δ in Sec. V. Section VI discusses the evolution of the essential charge and spin gaps across the AFCI phase. The paper is concluded in Sec. VII.

II. THE MODEL AND THE PHASE DIAGRAM

A. Hamiltonian

The Kane-Mele model [45] and the TRI Harper-Hofstadter model [46,47] have been introduced as two fundamental models to study the QSHI. The TRI Harper-Hofstadter model is simulated using ultracold atoms in optical lattices [48,49]. While the Kane-Mele model at half-filling represents a QSHI, the Harper-Hofstadter model at half-filling is a semimetal.

One needs to consider the Harper-Hofstadter model at other fillings or to add additional terms such as a NNN hopping to open a gap and achieve nontrivial topological states [50]. We include a NNN hopping to the TRI Harper-Hofstadter model and focus on half-filling. The half-filling is necessary to realize a Mott insulating phase in the presence of a strong Hubbard interaction and to make a comparison with the results of the Kane-Mele-Hubbard model [39].

A minimal extension of the TRI HHH model which allows to investigate the competition between the QSHI, the BI, and the Mott insulator states is thus given by

$$H = H_t + \Delta \sum_{\vec{r},\sigma} (-1)^{x+y} n_{\vec{r},\sigma} + U \sum_{\vec{r}} n_{\vec{r},\downarrow} n_{\vec{r},\uparrow} \tag{1}$$

with the hopping term

$$\begin{aligned} H_t = &-t \sum_{\vec{r}} (c^\dagger_{\vec{r}+\hat{x}} c_{\vec{r}} + c^\dagger_{\vec{r}+\hat{y}} e^{+2\pi i \varphi x \boldsymbol{\sigma}_z} c_{\vec{r}} + \text{H.c.}) \\ &- t' \sum_{\vec{r}} (c^\dagger_{\vec{r}+\hat{x}+\hat{y}} e^{+2\pi i \varphi (x+\frac{1}{2}) \boldsymbol{\sigma}_z} c_{\vec{r}} \\ &+ c^\dagger_{\vec{r}+\hat{y}} e^{+2\pi i \varphi (x+\frac{1}{2}) \boldsymbol{\sigma}_z} c_{\vec{r}+\hat{x}} + \text{H.c.}), \end{aligned} \tag{2}$$

where $\vec{r} = x\hat{x} + y\hat{y} = (x, y)$ runs over the square lattice with the lattice constant considered as the unit of length. The creation field operator at the lattice position $\vec{r}$ is given by $c^\dagger_{\vec{r}} = (c^\dagger_{\vec{r},\uparrow}, c^\dagger_{\vec{r},\downarrow})$. Similarly, the annihilation field operator is given by the column vector $c_{\vec{r}} = (c_{\vec{r},\uparrow}, c_{\vec{r},\downarrow})^T$. The index $\sigma = \uparrow, \downarrow$ specifies the z component of the particle spin. The occupation number operator reads as $n_{\vec{r},\sigma} = c^\dagger_{\vec{r},\sigma} c_{\vec{r},\sigma}$.

A particle picks up a phase determined by φ upon hopping which is opposite for opposite spins due to the Pauli matrix $\boldsymbol{\sigma}_z$, making the Hamiltonian time-reversal symmetric. We fix the phase parameter to $\varphi = \frac{1}{2}$ and the NNN hopping to $t' = 0.25t$ throughout this paper. The phase parameter $\varphi = \frac{1}{2}$ is the simplest case to achieve nontrivial topological bands. The second term in Eq. (1) is a checkerboard potential giving the onsite energy $+\Delta$ to sites with $x + y$ even and the onsite energy $-\Delta$ to sites with $x + y$ odd. It supports a BI phase in the system. The last term in Eq. (1) is the Hubbard interaction which describes the repulsion between particles with opposite spins occupying the same lattice site and at half-filling favors long-range AF order. The different terms in the Hamiltonian (1) for $\varphi = \frac{1}{2}$ are sketched schematically in the 2×2 unit cell in Fig. 1. We denote the four different sublattices as A_1 with x and y even, A_2 with x and y odd, B_1 with x odd and y even, and B_2 with x even and y odd.[1] The system has inversion symmetry where the center of inversion can be at any lattice site.

A clarification on the choice of the staggered potential in Eq. (1) is in order. We have considered a checkerboard potential changing as $\Delta(-1)^{x+y}$ and not a staggered potential changing only along one direction, e.g., $\Delta(-1)^x$. This is because in the presence of the checkerboard potential the effect of the time-reversal transformation on the Néel AF state cannot be compensated by a space-group operation while for the staggered potential along the x direction the effect of the time-reversal transformation on the Néel AF state can be compensated by a lattice shift along the y direction. The checkerboard potential permits the emergence of the Néel AFCI. The staggered potential changing only along the x direction can lead to other types of correlated topological states and we leave it for a future study. The Hamiltonian (1) with $\varphi = \frac{1}{2}$ is thus motivated as a minimal theoretical model which allows to investigate the AFCI phase beyond the noncentrosymmetric Kane-Mele-Hubbard model [39].

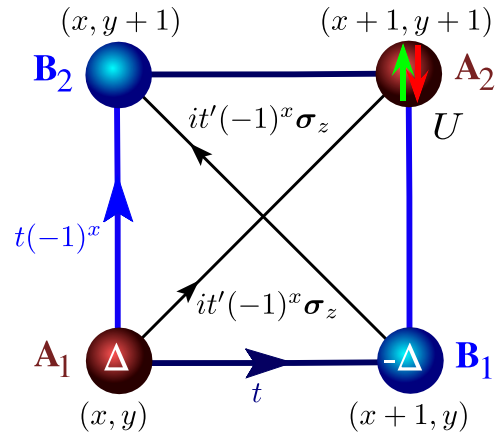

FIG. 1. Schematic representation of the Hamiltonian (1) for the phase parameter $\varphi = \frac{1}{2}$. The Hamiltonian involves a nearest-neighbor hopping t, a next-nearest-neighbor hopping t', a checkerboard potential Δ, and a Hubbard interaction U. Particles with opposite spins pick up opposite phases upon hopping due to the Pauli matrix $\boldsymbol{\sigma}_z$ in the phase factor. The different sublattices are labeled as A_1, A_2, B_1, and B_2.

B. Limiting behaviors

In the absence of the Hubbard interaction the Hamiltonian (1) reduces to a four-level problem in momentum space described by

$$H = \sum_{\vec{k},\sigma} \Phi^\dagger_{\vec{k},\sigma} \boldsymbol{\mathcal{H}}_\sigma(\vec{k}) \Phi_{\vec{k},\sigma} \tag{3}$$

with $\Phi_{\vec{k},\sigma} = (a_{1,\vec{k},\sigma}, b_{1,\vec{k},\sigma}, b_{2,\vec{k},\sigma}, a_{2,\vec{k},\sigma})^T$ where $a_{1,\vec{k},\sigma}$ is the Fourier transform of $c_{\vec{r},\sigma}$ on the sublattice A_1 and similarly for the other operators. The Bloch Hamiltonian is given by

$$\begin{aligned} \boldsymbol{\mathcal{H}}_\sigma(\vec{k}) = &(\Delta \boldsymbol{\sigma}_z - 2t \cos(k_y) \boldsymbol{\sigma}_x) \otimes \boldsymbol{\sigma}_z - 2t \cos(k_x) \mathbb{1} \otimes \boldsymbol{\sigma}_x \\ &+ 4t' \text{sgn}(\sigma) \sin(k_x) \sin(k_y) \boldsymbol{\sigma}_x \otimes \boldsymbol{\sigma}_y, \end{aligned} \tag{4}$$

where $\boldsymbol{\sigma}_x$, $\boldsymbol{\sigma}_y$, and $\boldsymbol{\sigma}_z$ stand for Pauli matrices and we have defined $\text{sgn}(\uparrow) = +1$ and $\text{sgn}(\downarrow) = -1$.

The energy bands of Eq. (4) are spin degenerate as $\boldsymbol{\mathcal{H}}_\uparrow(\vec{k})$ and $\boldsymbol{\mathcal{H}}_\downarrow(\vec{k})$ differ only by a transpose. This spin degeneracy originates from the time-reversal symmetry $\boldsymbol{\mathcal{H}}_\sigma(\vec{k}) = \boldsymbol{\mathcal{H}}^*_{\bar{\sigma}}(-\vec{k})$ and the inversion symmetry with respect to a lattice site $\boldsymbol{\mathcal{H}}_\sigma(\vec{k}) = \boldsymbol{\mathcal{H}}_\sigma(-\vec{k})$. We have used $\bar{\sigma}$ to indicate the opposite direction of σ.

[1] It is possible to reduce the number of sites in the unit cell to two sites by applying the spin-dependent local gauge transformation $c_{\vec{r}} \to e^{-i\pi \boldsymbol{\sigma}_z y^2/2} c_{\vec{r}}$. However, this shifts the energy bands in the momentum space and also changes the magnetic order in the large Hubbard U limit. We decided to avoid such a transformation to prevent potential confusion.

The Hamiltonian (4) at half-filling describes a QSHI for $\Delta < 4t'$ with the Chern numbers $\mathcal{C}_\uparrow = +1$ and $\mathcal{C}_\downarrow = -1$ for the up and down spins. Upon increasing Δ the gap closes at $\Delta = 4t'$ and for $\Delta > 4t'$ the system becomes a BI with $\mathcal{C}_\sigma = 0$ for both spin components. As we will show using the topological Hamiltonian method [51,52] a similar Hamiltonian but with a renormalized staggered potential determines the topological properties also of the interacting model (1).

In the large Hubbard U limit where the subspace with a finite number of doubly occupied sites is much higher in energy than the subspace with no double occupancy one can derive an effective spin Hamiltonian describing the low-energy properties of the system [53]. The effective spin Hamiltonian of the extended TRI HHH model (1) in the Mott limit $(U - 2\Delta) \gg t$ is given by

$$H_{\text{eff}} = J_1 \sum_{\langle i,j \rangle} \vec{S}_i \cdot \vec{S}_j + J_2 \sum_{[i,j]} \left(S_i^z S_j^z - S_i^x S_j^x - S_i^y S_j^y \right) \qquad (5)$$

with the NN $J_1 = 4t^2 U/(U^2 - 4\Delta^2)$ [54] and the NNN $J_2 = 4t'^2/U$ [55,56] exchange couplings. The notation $\langle i, j \rangle$ limits sites i and j to be NN and the notation $[i, j]$ limits sites i and j to be NNN. The spin anisotropy in the NNN exchange interaction stems from the spin-dependent NNN hopping which reduces the SU(2) symmetry to the U(1) symmetry. The Hamiltonian (5) supports the Néel AF state with a spin polarization in the x-y plane (xy-AF state) due to the ferromagnetic NNN exchange interaction in the x and y directions. This avoids the frustration induced by the AF NNN interaction in the z direction. The energy difference per lattice site of the Néel AF state with the spin polarization along the z direction (z-AF state) and the xy-AF state reads as

$$\varepsilon_z - \varepsilon_{xy} = J_2 = \frac{4t'^2}{U} \qquad (6)$$

in the mean-field approximation of the spin Hamiltonian (5). While in the Mott regime $(U - 2\Delta) \gg t$ the xy-AF state is the stable phase, we will show how charge fluctuations for $(U \sim 2\Delta) \gg t$ stabilize a z-AFCI.

A similar Hamiltonian as Eq. (1) but with hopping phases independent of spin, breaking explicitly the time-reversal symmetry, is employed in Ref. [36] to investigate the role of the lattice symmetry on the emergence of AF quantum Hall states. One notes that here we analyze systems which show spontaneous breaking of the time-reversal symmetry and the emergence of AFCIs. It is worth also mentioning that in the absence of the hopping phase, i.e., for $\varphi = 0$, and vanishing NNN hopping $t' = 0$, the Hamiltonian in Eq. (1) reduces to the ionic Hubbard model which has been used as a paradigmatic model for studying the transition from band to Mott insulator in one [54,57–60] and two [61–66] dimensions.

C. Phase diagram

Before proceeding to the technical aspects and discussing the results in details we present the phase diagram of the extended TRI HHH model (1) for the phase parameter $\varphi = \frac{1}{2}$ and the NNN hopping $t' = 0.25t$ in the U-Δ plane in Fig. 2. We have used DMFT [44] and the topological Hamiltonian method [51,52] to address the effect of the interaction. The system is a QSHI for small values of Δ and the Hubbard interaction induces a transition to the xy-AF phase. For intermediate values of Δ the system is in the BI phase and the Hubbard interaction first drives the system into the QSHI and then into the xy-AF state. For large values of Δ, a z-AFCI separates the BI from the xy-AF phase. We cannot exclude the possible existence of an extremely narrow trivial z-AF phase between the BI and the z-AFCI. The positions of the tricritical points in Fig. 2 are approximate as their accurate determination is demanding. The phase diagram 2 is obtained for the small but finite temperature $T = 0.02t$ to guarantee that the narrow z-AFCI phase can survive thermal fluctuations and be found in a real experiment which is always performed at a finite T.

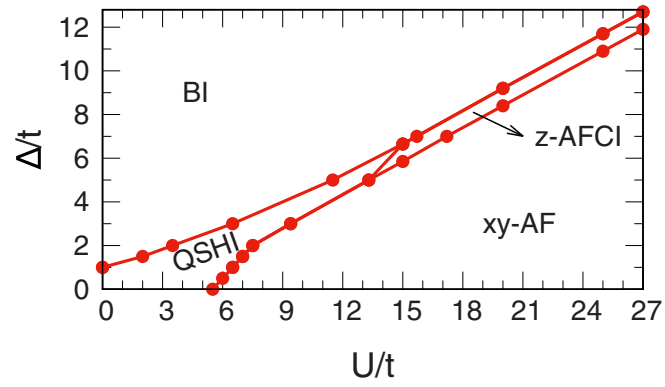

FIG. 2. The phase diagram of the extended time-reversal-invariant Harper-Hofstadter-Hubbard model in Eq. (1) for the phase parameter $\varphi = \frac{1}{2}$ and the next-nearest-neighbor hopping $t' = 0.25t$. The phase diagram involves a trivial band insulator (BI), a quantum spin Hall insulator (QSHI), a Néel antiferromagnetic state with the spin polarization in the xy plane (xy-AF), and a Néel antiferromagnetic Chern insulator with the spin polarization along the z direction (z-AFCI). The results are for the temperature $T = 0.02t$.

The similarity between the phase diagram in Fig. 2 and the phase diagram of the noncentrosymmetric Kane-Mele-Hubbard model [39] suggests that the z-AFCI is not a phase limited to a specific model or a specific lattice structure, but rather is a generic consequence of strong electronic correlation and spin-orbit coupling in two-dimensional systems. The necessary condition to realize an AFCI is the absence of a space-group operation to compensate the effect of the time-reversal transformation on the electronic state which can be achieved with or without the inversion symmetry. Our DMFT analysis demonstrates that the z-AFCI can exist beyond the (slave boson) mean-field approximation [39] and survives local quantum fluctuations.

III. TECHNICAL ASPECTS

A. Dynamical mean-field theory

We employ DMFT which is an established approach to systems with strong local interaction and large coordination number. The method approximates the self-energy to be spatially local which is exact in the limit of infinite coordination number. In the case of finite coordination number the nonlocal quantum fluctuations due to the momentum dependence of the self-energy are neglected. The local quantum fluctuations are

fully taken into account. The lattice model is mapped to an Anderson impurity model determined self-consistently [44]. DMFT has been extensively applied in the past decade to interacting two-dimensional topological systems [36,37,47,67–71].

We use real-space DMFT [72–74] as it allows access not only to the bulk, but also to the edges of the system. The self-energy is local but it can depend on the position

$$\Sigma_{\vec{r},\sigma;\vec{r}',\sigma'}(i\omega_n) = \delta_{\vec{r},\vec{r}'}\Sigma_{\vec{r};\sigma,\sigma'}(i\omega_n)\,. \tag{7}$$

One notes that the spin off-diagonal elements of the self-energy $\Sigma_{\vec{r};\sigma,\bar{\sigma}}(i\omega_n) \neq 0$ are essential to describe the xy-AF phase. We use our implementation of real-space DMFT for SU(N) systems introduced in Ref. [75] due to its easy adaptability to different models and its capability of addressing self-energies with spin off-diagonal elements. We use the exact diagonalization (ED) method as the impurity solver which provides an accurate description of static local quantities and permits direct access to real-frequency dynamical quantities [76].

We mainly consider 40×40 lattices with periodic boundary conditions to investigate the bulk properties. However, near phase transitions especially in the z-AFCI region we have performed calculations also for 60×60 lattices and find no change in the results. To analyze edge excitations, 41×40 lattices are used with open boundary conditions along x and periodic boundary conditions along y direction, i.e., cylindrical geometry. One notes that although we use the real-space DMFT we fully exploit the translational symmetry of the system to set up the impurity problem and to compute the lattice Green's function [75]. For example, for the bulk properties the impurity model is addressed only at the four lattice sites in the unit cell sketched in Fig. 1.

We mainly use the number of bath sites $n_{\rm bs} = 6$ in the effective Anderson impurity problem. However, we will present data also for $n_{\rm bs} = 5$, 7, and 8 across the z-AFCI phase and show that the results obtained for these different numbers of bath sites are almost indistinguishable. This stems from the perfect description of the dynamical Weiss field we find in all these cases. The conservation of the total z component of spin is used in the ED except for the xy-AF phase. We fix the temperature to $T = 0.02t$ and perform the DMFT loop with 200 positive Matsubara frequencies. Again, we pay careful attention to the z-AFCI region where we increase the number of positive Matsubara frequencies up to 1000. A chemical potential μ is added to the Hamiltonian (1) and is adjusted within the DMFT loop to satisfy the half-filling condition.

B. Topological Hamiltonian method

Although the real-space DMFT makes it possible to directly spot the excitations at the bulk and at the edges, a more precise way to determine the topological phase transitions is by computing the topological invariants. For an interacting system, the topological invariants can be calculated using twisted boundary conditions [77]. This requires knowledge of the eigenstates of the system which is beyond the scope of the DMFT. Topological invariants can be expressed also based on the Green's function provided the system contains no nontrivial degeneracy, such as the one in fractional quantum Hall states [78,79]. Such a condition is satisfied for all the phases we investigate in this paper. The method involves frequency and momentum integrations over the Green's function and its derivatives and remains computationally demanding. In Ref. [51] it has been shown by adiabatic deformation of the imaginary-frequency Green's function (such that the charge gap never closes) that the topological invariant of an interacting system can be determined from an effective noninteracting model. The method is exact provided that the necessary conditions are satisfied [52]. The effective model, called topological Hamiltonian, in the Bloch form reads as

$$\boldsymbol{\mathcal{H}}_{\rm t}(\vec{k}) = \boldsymbol{\mathcal{H}}_0(\vec{k}) + \boldsymbol{\Sigma}(\vec{k}, \omega = 0), \tag{8}$$

where $\boldsymbol{\mathcal{H}}_0(\vec{k})$ is the noninteracting part of the Hamiltonian and $\boldsymbol{\Sigma}(\vec{k}, 0)$ is the self-energy in momentum space and at zero frequency.

It should be mentioned that the topological invariant can change not only due to the poles of the Green's function but also due to its zeros [80], e.g., in paramagnetic Mott insulators where the self-energy at zero frequency diverges [27]. But this does not occur in the phases studied in this paper.

The noninteracting part of the Hamiltonian (1) in the Bloch representation is given by Eq. (4). The self-energy in the DMFT is local. Hence, the momentum-space self-energy in the paramagnetic and in the z-AF state is given by

$$\begin{aligned}\boldsymbol{\Sigma}_\sigma(\vec{k}, 0) = &+\tfrac{1}{2}(\Sigma_{A,\sigma}(0) + \Sigma_{B,\sigma}(0))\mathbb{1} \otimes \mathbb{1} \\ &+ \tfrac{1}{2}(\Sigma_{A,\sigma}(0) - \Sigma_{B,\sigma}(0))\boldsymbol{\sigma}_z \otimes \boldsymbol{\sigma}_z,\end{aligned} \tag{9}$$

where $\Sigma_{A,\sigma}(0)$ is the self-energy on the sublattice with the higher onsite energy and $\Sigma_{B,\sigma}(0)$ is the self-energy on the sublattice with the lower onsite energy. One notes that the self-energy on the sublattices A_1 and A_2 are equal, and also on the sublattices B_1 and B_2.

The topological Hamiltonian obtained by adding the self-energy (9) to the Bloch Hamiltonian (4) remains, up to an irrelevant constant, the same as Eq. (4) but with the renormalized staggered potential

$$\tilde{\Delta}_\sigma = \Delta + \tfrac{1}{2}(\Sigma_{A,\sigma}(0) - \Sigma_{B,\sigma}(0)). \tag{10}$$

We drop the lower index σ when discussing paramagnetic phases as there is no spin dependence. The system is in the QSHI phase for $|\tilde{\Delta}| < 4t'$ and in the BI phase for $|\tilde{\Delta}| > 4t'$. In the z-AF state, however, the renormalized staggered potential (10) depends on the spin and, in principle, it is possible that one spin component falls in the topological region $|\tilde{\Delta}_\sigma| < 4t'$ and the other in the trivial region $|\tilde{\Delta}_\sigma| > 4t'$. This leads to the emergence of a CI. For the NNN hopping $t' = 0.25t$ that we consider throughout this paper the topological transition occurs at $|\tilde{\Delta}_\sigma| = t$.

The renormalized staggered potential in Eq. (10) requires the self-energy at zero frequency. We always find that the value of the real part of the self-energy at the smallest Matsubara frequency $\omega_0 = \pi T$ perfectly describes the value of the self-energy at zero frequency obtained by a polynomial extrapolation. This means one can replace $\Sigma_{A,\sigma}(0)$ with $\mathrm{Re}[\Sigma_{A,\sigma}(\omega_0)]$ and $\Sigma_{B,\sigma}(0)$ with $\mathrm{Re}[\Sigma_{B,\sigma}(\omega_0)]$ in Eq. (10).

The DMFT together with the topological Hamiltonian method have been used extensively to map out the phase

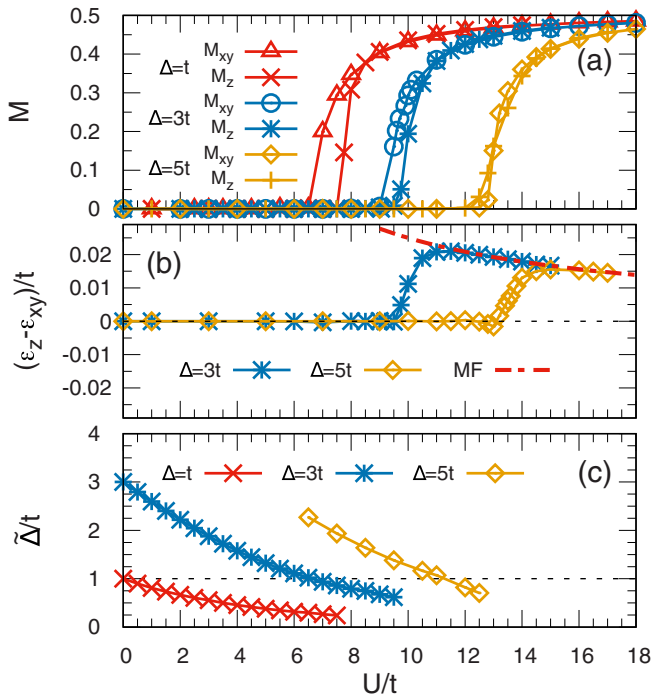

FIG. 3. (a) The local spin polarization in the xy-AF state (M_{xy}) and in the z-AF state (M_z) vs the Hubbard interaction U for different values of the staggered potential Δ. (b) The energy difference per lattice site of the z-AF state and the xy-AF state vs the Hubbard U for $\Delta = 3t$ and $5t$. The mean-field result (6) of the effective low-energy spin model is included as a red dashed line for comparison. (c) The renormalized staggered potential $\tilde{\Delta}$ in the paramagnetic region vs the Hubbard U for different values of Δ. The system is in the trivial band insulator for $\tilde{\Delta} > t$ and in the quantum spin Hall insulator for $\tilde{\Delta} < t$ which are separated by the dashed line at $\tilde{\Delta} = t$. The results shown are for the number of bath sites $n_{\rm bs} = 6$.

diagram of various interacting topological systems [36,37,67–70,81]. The phase diagram of the Haldane-Hubbard model obtained using the DMFT and the topological Hamiltonian method agrees qualitatively with the results obtained using ED and twisted boundary conditions [37]. A systematic study of the quantum fluctuations beyond the DMFT indicates small changes to the phase boundaries [82]. Similarly, we expect our phase diagram to be qualitatively reliable, i.e., to be reliable with regard to the types of the phases present and to which phase is adjacent to which other phase. But the position of the phase boundaries might be shifted upon including the nonlocal quantum fluctuations.

IV. WEAK TO INTERMEDIATE STAGGERED POTENTIALS

In Fig. 3(a) the local spin polarization in the z-AF state (M_z) and in the xy-AF state (M_{xy}) is plotted vs the Hubbard interaction U for the staggered potential $\Delta = t$, $3t$, and $5t$, which correspond to small and intermediate values of Δ in the phase diagram 2. The results are for the number of bath sites $n_{\rm bs} = 6$ in the ED impurity solver. The local spin polarizations are given by

$$M_z = \tfrac{1}{2}|\langle c^\dagger_{\vec{r}}\, \boldsymbol{\sigma_z}\, c_{\vec{r}}\rangle|, \tag{11a}$$

$$M_{xy} = \tfrac{1}{2}|\langle c^\dagger_{\vec{r}}\, \boldsymbol{\sigma_x}\, c_{\vec{r}}\rangle\hat{x} + \langle c^\dagger_{\vec{r}}\, \boldsymbol{\sigma_y}\, c_{\vec{r}}\rangle\hat{y}|. \tag{11b}$$

The lattice has the Néel AF order. The xy-AF phase is continuously degenerate due to the spontaneous breaking of the U(1) symmetry. We have produced multiple xy-AF solutions for the DMFT equations corresponding to the local spin polarization vector pointing in different directions in the x-y plane. We find all the solutions having the same local spin polarization M_{xy} and the same energy. This serves as a corroborating test for our results. The z-AF solution is twofold degenerate due to the spontaneous breaking of the time-reversal symmetry.

The xy-AF state and the z-AF state in Fig. 3(a) show the same local spin polarization at large values of U. However, the spin polarizations M_{xy} and M_z become distinct as the Hubbard U is reduced. For small values of the staggered potential Δ the xy-AF state persists to smaller values of U compared to the z-AF state. As one can see for $\Delta = t$ in Fig. 3(a) the spin polarization in the z-AF state vanishes at $U \sim 7.5t$ while the spin polarization in the xy-AF state survives down to $U \sim 6.5t$. This enhanced robustness of the xy-AF phase over the z-AF phase against the charge fluctuations reduces upon increasing the staggered potential to $\Delta = 3t$ and disappears for $\Delta = 5t$.

We have compared the energy per site of the z-AF (ε_z) and the xy-AF (ε_{xy}) states in Fig. 3(b) for $\Delta = 3t$ and $5t$. One can see that the xy-AF state has a lower energy compared to the z-AF state. This is what one would naturally expect in the Mott regime based on the effective spin model (5). We expect our DMFT treatment in the Mott limit to be equivalent to the mean-field approximation of the low-energy spin model (5). This is because the local quantum fluctuations taken into account in the DMFT influence only the high-energy properties, which are already eliminated in the derivation of the spin model. The spin model only involves nonlocal quantum fluctuations. Such an equivalence can also be seen for the Néel temperature of the Hubbard model [83]. The energy difference in Fig. 3(b) for large Hubbard interactions approaches the mean-field result of the spin model given by Eq. (6) with $t' = 0.25t$, independent from Δ. The mean-field results are denoted in Fig. 3(b) by a dashed red line. One notes that although in the Mott regime $(U - 2\Delta) \gg t$ the DMFT results equal the mean-field results of the effective low-energy spin model, the DMFT analysis takes into account the charge fluctuations which become essential as the Hubbard interaction is reduced. We will show how these charge fluctuations for $(U \sim 2\Delta) \gg t$ favor energetically the z-AF state over xy-AF state. Evidence of the z-AF phase acquiring an energy lower than the xy-AF phase can already be seen in Fig. 3(b) for $\Delta = 5t$ near $U = 13t$. This becomes more pronounced as Δ is further increased in Sec. V. One notes that the location of the tricritical points in the phase diagram 2 is only approximate as they are difficult to be determined accurately.

In order to identify the transition between the BI and the QSHI in the paramagnetic region the renormalized staggered potential (10) is plotted in Fig. 3(c) vs the Hubbard U for

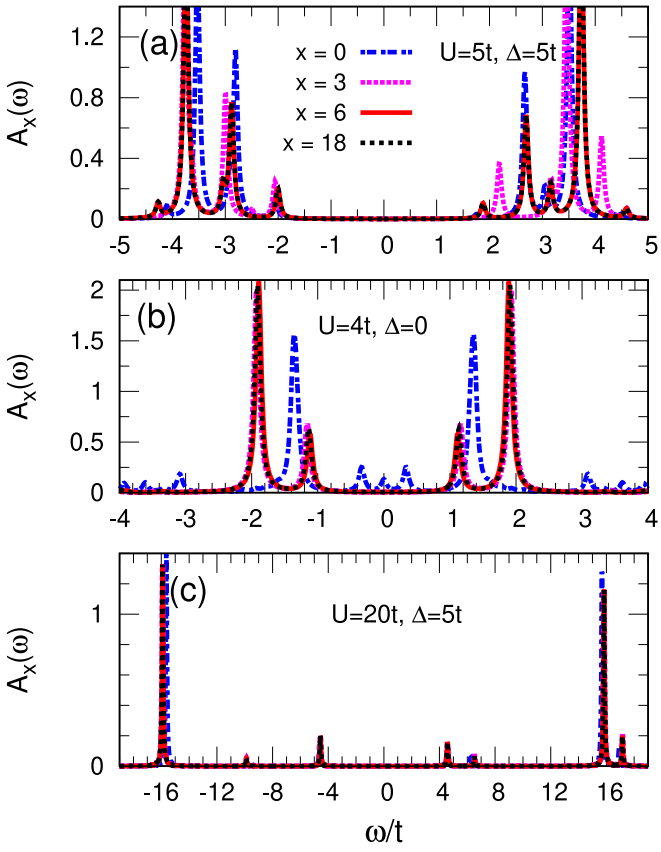

FIG. 4. The spectral function $A_x(\omega)$ given by Eq. (12) vs frequency for a cylinder of the size 41×40 with the edges at $x = 0$ and at $x = 40$ in the trivial band insulator phase for $U = 5t$ and $\Delta = 5t$ (a), in the quantum spin-Hall insulator phase for $U = 4t$ and $\Delta = 0$ (b), and in the Néel antiferromagnetic phase with the spin polarization in the x-y plane for $U = 20t$ and $\Delta = 5t$ (c). The results are symmetric with respect to the middle $x = 20$ of the cylinder. The results are obtained for the number of bath sites $n_{\rm bs} = 6$.

the different values of the staggered potential $\Delta = t$, $3t$, and $5t$. For $\Delta = t$ the system is at the phase boundary of the BI and the QSHI for $U = 0$. As the Hubbard U is increased the renormalized staggered potential $\tilde{\Delta}$ lowers and the system becomes a QSHI. For $\Delta = 3t$ and $5t$ the system for small values of U is in the BI phase with $\tilde{\Delta} > t$. As the Hubbard U is increased, the renormalized staggered potential crosses the dashed line at $\tilde{\Delta} = t$ and the transition to the QSHI takes place.

The real-space DMFT permits to spot bulk and edge excitations of the interacting system by considering cylindrical geometries. Although due to the finite number of bath sites in the ED impurity solver the spectral function is not smooth consisting of separate sharp peaks, it can still signal the existence of gapless excitations at the edges [36,70]. This is observed also for the ED of lattice models [84]. Figure 4 displays the spectral function resolved along the x direction $A_x(\omega)$ for a cylinder of the size 41×40 with the edges at $x = 0$ and at $x = 40$. The results in Fig. 4 correspond to the BI phase for $U = 5t$ and $\Delta = 5t$ (a), to the QSHI phase for $U = 4t$ and $\Delta = 0$ (b), and to the xy-AF phase for $U = 20t$ and $\Delta = 5t$ (c). The spectral function $A_x(\omega)$ is given by

$$A_x(\omega) = \frac{1}{4} \sum_{\sigma} [A_{x,y;\sigma}(\omega) + A_{x,y+1;\sigma}(\omega)], \qquad (12)$$

where $A_{x,y;\sigma}(\omega)$ is the spectral function at the lattice position (x, y) for the spin σ. One notes that $A_x(\omega)$ does not depend on y and σ as we average over the two sites in the unit cell in the y direction and over the spin. We have limited the x coordinate in Fig. 4 to $x < 20$ as the results are symmetric with respect to the middle $x = 20$ of the cylinder. The spectral function in Eq. (12) averaged over the spin and the periodic y direction but resolved along the open x direction allows us to examine how the charge excitations change from the bulk to the edge of the system. The results are for the number of bath sites $n_{\rm bs} = 6$. A Lorentzian broadening with the broadening factor $0.05t$ is used in the calculations.

As one can see from Fig. 4(b) there are gapless excitations at the edges which quickly disappear as the bulk is approached. In contrast, we find gapped excitations in the bulk and at the edges in Figs. 4(a) and 4(c). As we move away from the edges, the results in all the panels in Fig. 4 perfectly coincide with the bulk results $x = 18$. Figure 4 allows us to directly investigate the topological and the trivial nature of the different phases in the interacting system without using the topological Hamiltonian method, if we assume that the bulk-boundary correspondence is valid. However, one notes that this approach is only accurate when the system is deep within a phase, where the edge excitations are either gapless as in Fig. 4(b) or there is a large energy gap as in Figs. 4(a) and 4(c). Near the phase boundaries one needs a high-resolution energy spectrum to distinguish a gapless spectrum from a spectrum which has a tiny energy gap. In our analysis, the energy resolution is limited by the finite number of bath sites in the ED impurity solver. To determine the topological phase boundaries accurately one needs to use the topological Hamiltonian method and compute the topological invariants which change abruptly at a transition point.

V. ANTIFERROMAGNETIC CHERN INSULATOR

Up to now our discussion of the phase diagram in Fig. 2 has been limited to small and intermediate values of Δ with $\Delta \leqslant 5t$. In the following we will focus on large values of Δ where a z-AFCI appears between the BI and the xy-AF phases.

In Fig. 5(a) the local spin polarizations in the z-AF and in the xy-AF states are depicted vs the Hubbard U for the staggered potential $\Delta = 7t$. The number of bath sites is given by $n_{\rm bs} = 6$. Comparing with the results in Fig. 3(a) one can see how a region with a finite M_z and zero M_{xy} develops upon increasing the value of Δ. The energy difference between the z-AF state and the xy-AF state plotted vs U for $\Delta = 7t$ in Fig. 5(b) shows that the z-AF state becomes the stable phase with $\varepsilon_z < \varepsilon_{xy}$ before M_{xy} vanishes. A very similar spin-flop phase transition between the xy-AF order and the z-AF order is observed in the Kane-Mele-Hubbard model [39]. The phase diagram of the Kane-Mele-Hubbard model is investigated also in Ref. [85]. However, the analysis in Ref. [85] is limited to small values of the sublattice potential and the z-AF state is never found as the stable phase.

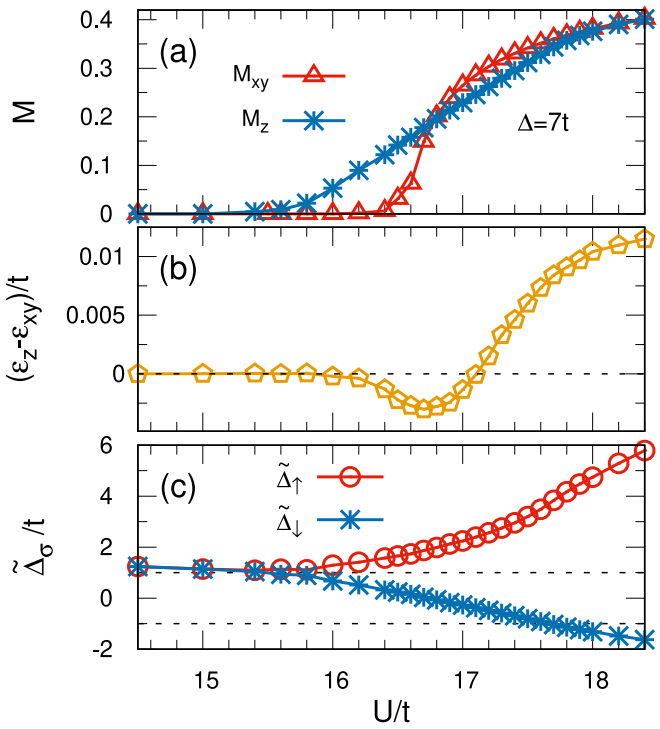

FIG. 5. (a) The local spin polarization in the xy-AF state (M_{xy}) and in the z-AF state (M_z) vs the Hubbard interaction U. (b) The energy difference per lattice site of the z-AF state and the xy-AF state vs U. (c) The renormalized staggered potential $\tilde{\Delta}_\sigma$ defined by Eq. (10) in the z-AF phase vs the Hubbard U. The dashed lines in (c) separate the topological region $|\tilde{\Delta}_\sigma| < t$ from the trivial region $|\tilde{\Delta}_\sigma| > t$. The results are for the staggered potential $\Delta = 7t$. We have used the number of bath sites $n_{\rm bs} = 6$ in the ED impurity solver. The results in (c) are for the magnetic solution with the spin-up particles occupying mainly the lower-energy sublattice.

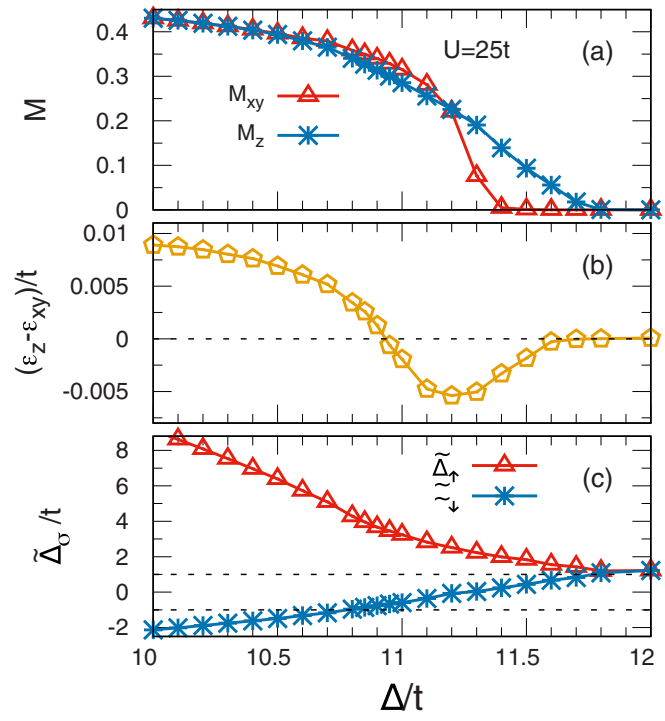

FIG. 6. The same quantities as in Fig. 5 but for the fixed Hubbard interaction $U = 25t$ and varying staggered potential Δ.

To address the topological properties of the z-AF phase we have plotted the renormalized staggered potential (10) vs the Hubbard interaction in Fig. 5(c) for $\Delta = 7t$. The dashed lines separate the topological $|\tilde{\Delta}_\sigma| < t$ from the trivial $|\tilde{\Delta}_\sigma| > t$ region. In the paramagnetic regime for $U < 15.5t$ the renormalized staggered potential $\tilde{\Delta}_\sigma$ is independent of the spin and $\tilde{\Delta}_\sigma > t$ suggests a BI phase. At $U \approx 15.5t$ we find $\tilde{\Delta}_\sigma$ extremely close to t. As the system enters the z-AF phase for $U > 15.5t$ the renormalized staggered potential $\tilde{\Delta}_\sigma$ becomes spin dependent, increasing for one spin component and decreasing for the other. One spin component falls in the trivial region $|\tilde{\Delta}_\sigma| > t$ and the other in the topological region $|\tilde{\Delta}_\sigma| < t$. The results provided in Fig. 5(c) correspond to the z-AF solution with the lower-energy sublattice occupied mainly with spin-up particles. Figure 5(c) demonstrates that the z-AF state has a finite Chern number and the emergence of the z-AFCI.

To further check the existence of the z-AFCI between the BI and the xy-AF phase for $(U \sim 2\Delta) \gg t$ we have investigated in Fig. 6 the same quantities as in Fig. 5 but for the fixed Hubbard interaction $U = 25t$, varying the staggered potential Δ. One can see a very similar behavior as in Fig. 5. The z-AF phase is stable for $10.9t \lesssim \Delta \lesssim 11.8t$ with one spin component in the topological region $|\tilde{\Delta}_\sigma| < t$ and the other in the trivial region $|\tilde{\Delta}_\sigma| > t$. Similar to Fig. 5 we find that at the point where M_z vanishes the renormalized staggered potential $\tilde{\Delta}_\sigma$ is very close to t. However, we note that we cannot in essence rule out the existence of an extremely narrow trivial z-AF phase between the BI and the z-AFCI which corresponds to a renormalized staggered potential $\tilde{\Delta}_\sigma$ being slightly above t rather than being *exactly* at t at the point where M_z vanishes.

We have carried out the same analysis as in Fig. 6 also for the Hubbard interactions $U = 15t$, $20t$, and $27t$ and the obtained transition points are specified in the phase diagram Fig. 2. Figure 2 exhibits a constant width proportional to t for the z-AFCI as the atomic limit $U/t, \Delta/t \to \infty$ is approached. In the phase diagram of the Kane-Mele-Hubbard model obtained using mean-field theory, the width of the z-AFCI phase increases as the Hubbard U and the sublattice potential Δ are increased [39]. In the slave-boson mean-field analysis of the Kane-Mele-Hubbard model, however, a constant width for the z-AFCI phase is found [39] quite comparable to our results in Fig. 2. This close similarity of the results obtained for these two different models shows that the AFCI is a robust phase which can emerge between the BI and the trivial AF Mott insulator independent from the details of the system. What is essential is the presence of the spin-orbit coupling and the absence of a space-group operation that could compensate the effect of the time-reversal transformation on the electronic state.

To show that the number of bath sites in the impurity solver does not alter our results we have compared in Fig. 7 the local spin polarizations M_{xy} (a) and M_z (b) for $n_{\rm bs} = 6$ at selective points across the z-AFCI phase with the results obtained for $n_{\rm bs} = 5$, 7, and 8. The results are for the Hubbard interaction

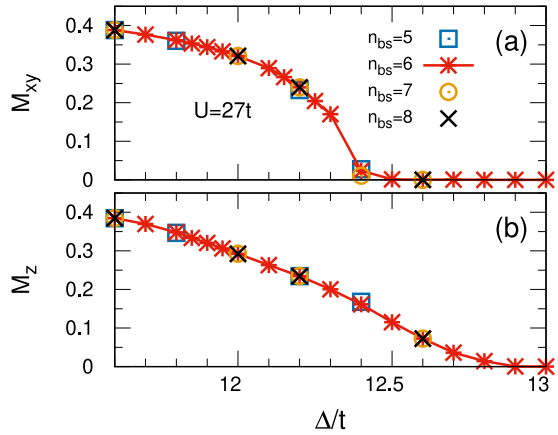

FIG. 7. Comparison of the local spin polarizations obtained for different number of bath sites $n_{\rm bs}$ in the ED impurity solver for the Hubbard interaction $U = 27t$ and varying staggered potential Δ across the z-AFCI phase. (a), (b) Display the local spin polarizations in the xy-AF state (M_{xy}) and in the z-AF state (M_z).

$U = 27t$. One can hardly see any change in the data upon changing the number of bath sites.

VI. ANTIFERROMAGNETIC CHERN INSULATOR FROM GAP-CLOSING PERSPECTIVE

As the staggered potential Δ is increased in Fig. 6(c) the spin-up component remains in the trivial region while the spin-down component undergoes a transition from the trivial to the topological region. Such a transition requires closing of the charge gap. Hence, the charge excitations for the different spin components are expected to show different behaviors. To see how the charge excitations in the system depend on the spin we plot the spin-resolved spectral function

$$A_\sigma(\omega) = \frac{1}{4} \sum_{(x,y)\in \text{unit cell}} A_{x,y;\sigma}(\omega) \tag{13}$$

in Fig. 8. The sum in Eq. (13) runs over the 2×2 unit cell specified in Fig. 1. The results in Fig. 8 are given for $U = 25t$ and the number of bath sites $n_{\rm bs} = 8$. Similar to the results in Fig. 6(c), the results in Fig. 8 are for the magnetic solution with the lower-energy sublattice mainly occupied with spin-up particles [see Fig. 9(a) for a schematic sketch of the state]. The magnetic results in Fig. 8 are always given for the z-AF solution, even for the small values of $\Delta = 6t$ in Fig. 8(a) and $\Delta = 8t$ in Fig. 8(b) where the z-AF state is metastable [see Fig. 6(b)]. We avoid the spin-flop transition because our aim in this section is to study the stabilization of the z-AFCI phase from the perspective of gap closing, i.e., to study how the charge gap continuously changes as Δ is increased in Fig. 6(c) and the transition to the z-AFCI phase takes place.

The staggered potentials $\Delta = 6t$ and $8t$ in Figs. 8(a) and 8(b) correspond to a highly polarized z-AF phase with both spin components in the trivial region. For the fully polarized state the charge excitation for the spin up corresponds to moving a particle from the lower-energy sublattice to the higher-energy sublattice [see Fig. 9(a)]. This costs an energy equal to $U + 2\Delta$. This nicely explains the spectral weights

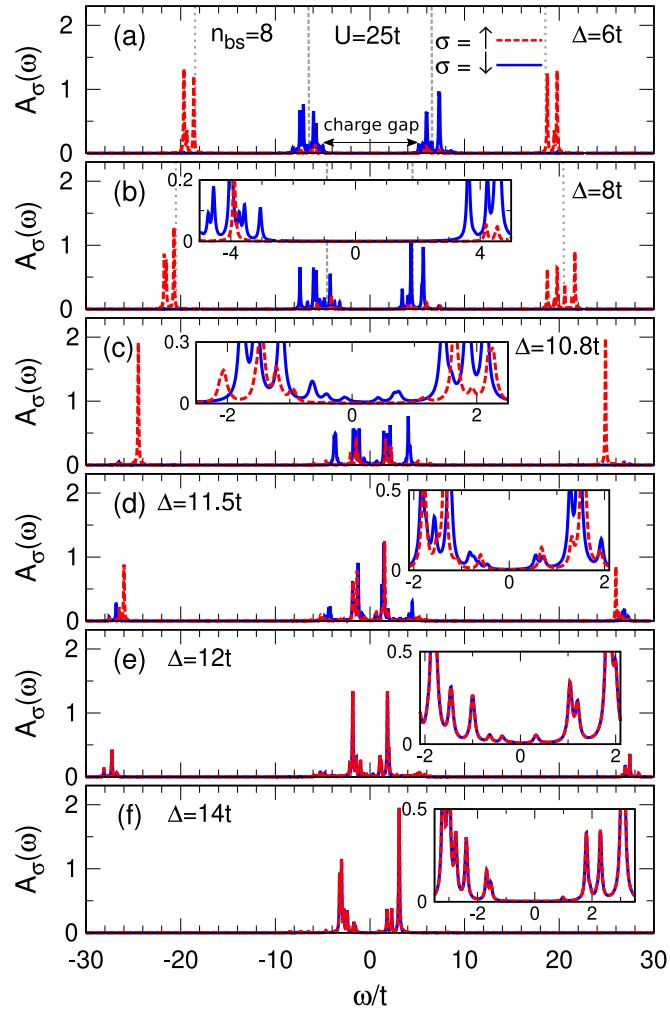

FIG. 8. The spin-resolved spectral function $A_\sigma(\omega)$ given by Eq. (13) vs frequency for the Hubbard interaction $U = 25t$ and different values of the staggered potential Δ across the z-AFCI phase. The results in (a) to (d) correspond to the z-AF solution with the lower-energy sublattice mainly occupied with spin-up particles [see (a) in Fig. 9]. The results are for the number of bath sites $n_{\rm bs} = 8$ in the ED impurity solver.

for spin up in Figs. 8(a) and 8(b) distributed mainly near $\omega = \pm(U/2 + \Delta)$. The points $\omega = \pm(U/2 + \Delta)$ in Figs. 8(a) and 8(b) are specified by vertical dotted lines. The charge excitation for spin down corresponds to moving a particle from the higher-energy sublattice to the lower-energy sublattice, which costs an energy equal to $U - 2\Delta$. This explains the spectral weight distribution for spin down appearing around $\omega = \pm(U/2 - \Delta)$ in in Figs. 8(a) and 8(b). The points $\omega = \pm(U/2 - \Delta)$ in Figs. 8(a) and 8(b) are specified by vertical dashed lines. One notes that near $\omega = \pm(U/2 - \Delta)$ there are also some spectral weights for spin up which can more obviously be seen from the inset in Fig. 8(b). These contributions are important because they define the charge gap for the spin up and originate from the fact that the system is not fully polarized.

The charge gap is defined by the energy difference of the electron and the hole spectral peaks closest to the Fermi energy $\omega = 0$. The charge gap is specified by a double-head

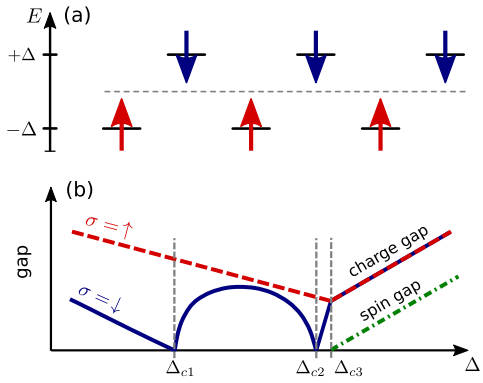

FIG. 9. (a) Schematic representation of an AF state with the spin-up sublattice having a lower onsite energy ($E = -\Delta$) in contrast to the spin-down sublattice ($E = +\Delta$). (b) Schematic representation of the charge gap for the spin up ($\sigma = \uparrow$) and the spin down ($\sigma = \downarrow$) vs the staggered potential Δ across the z-AFCI. The sketch corresponds to the z-AF solution in which the sublattice with the lower onsite energy is mainly occupied with spin-up particles, as shown in (a). The spin gap in the trivial band insulator phase, corresponding to $\Delta > \Delta_{c3}$, is also shown in (b). The spin gap stems from an electron-hole bound state with the total spin $S = 1$ and the magnetic polarization $\alpha = z$ (see the main text). The local spin polarization M_z becomes finite for $\Delta < \Delta_{c3}$ upon closing the spin gap. The Chern number $\mathcal{C}_\sigma$ changes upon closing the charge gap for the spin component σ. The Chern number is finite only for $\Delta_{c1} < \Delta < \Delta_{c2}$.

arrow in Fig. 8(a). Figures 8(a) and 8(b) show that the charge gap for the spin down is always smaller than the charge gap for the spin up. The charge gap for both spin components decreases as the staggered potential Δ is increased approaching the transition point to the z-AFCI. According to Fig. 6(c) the spin-down component undergoes a transition from the trivial state to the topological state at $\Delta = 10.8t$. Figure 8(c) displays the spin-resolved spectral function for the same value of Δ. As one can see from the inset in Fig. 8(c) there are some spectral contributions near the Fermi energy for the spin-down component while the spin-up component is clearly gapped. This is nicely consistent with the expectation that the change of the Chern number is accompanied by closing of the charge gap.

For the staggered potential $\Delta = 11.5t$ in Fig. 8(d) the system is within the z-AFCI. The spectral weight distribution for the spin up shows a manifest shift of the spectral weights from $\omega \approx \pm(U/2 + \Delta)$ to $\omega \approx \pm(U/2 - \Delta)$ in contrast to the spectral weight distribution for small values of Δ. This is due to the noticeable reduction of the local spin polarization M_z and approaching the paramagnetic region as can be seen from Fig. 6(a). The inset in Fig. 8(d) suggests a finite and rather equal charge gap for both spin components. This finite charge gap corroborates the insulating bulk state for both spin components. For the staggered potential $\Delta = 12t$ in Fig. 8(e) the system enters the paramagnetic phase and the spectral functions for up and down spins coincide. We observe an increase in the charge gap upon increasing the staggered potential from $\Delta = 12t$ in Fig. 8(e) to $\Delta = 14t$ in Fig. 8(f) which signals a BI phase consistent with our finding based on the renormalized staggered potential in Fig. 6(c).

Although it is not possible to extract from the ED spectral functions quantitative values for the charge gap which changes smoothly across the narrow z-AFCI region, a qualitative behavior can still be concluded. One should note that apart from the finite number of bath sites in our ED impurity solver, it is inherently difficult to obtain accurate results especially for dynamical quantities near a critical region. Figure 9(b) shows schematically how the different phase transitions take place upon changing the staggered potential across the z-AFCI from the gap-closing perspective. In addition to the charge gap for the up and the down spins the figure includes also the spin gap in the BI phase. The spin gap is the excitation energy of an electron-hole bound state with the total spin $S = 1$. It is the condensation of such a bound state which leads to the stabilization of an AF order. The stabilization of an AF state upon softening an $S = 1$ excitation is well known in dimerized magnetic systems [86–90]. It can also be seen from the analysis of various gaps for the ionic Hubbard model [66] as an electronic model similar to our Hamiltonian in Eq. (1). One should note, however, that there is a spin-dependent hopping phase in Eq. (1) which lifts the degeneracy between the magnetic number $m = 0$ and the magnetic numbers $m = \pm 1$, or equivalently in terms of a specific magnetic polarization $\alpha = x, y, z$ [86], the degeneracy between the magnetic polarization $\alpha = z$ and the magnetic polarizations $\alpha = x, y$. It is the magnetic polarization $\alpha = z$ which defines the spin gap in Fig. 9(b) and stabilizes the z-AF state [86]. In sketching the charge gap for the up and the down spins in Fig. 9(b) it is supposed that the spin-up sublattice has the lower onsite energy in contrast to the spin-down sublattice [see Fig. 9(a)].

Starting from the limit of large values of Δ in Fig. 9(b) the system is in the BI phase with an identical charge gap for the up and the down spins. Upon decreasing Δ the spin gap vanishes at Δ_{c3} and the system acquires a z-AF order for $\Delta < \Delta_{c3}$. The charge gap becomes spin dependent in the magnetically ordered phase. This is due to the fact that the effect of the time-reversal transformation on the z-AF state cannot be compensated by a space-group operation. Otherwise, the charge gap would remain equal for the up and the down spins even in a magnetically ordered phase. This would prevent the different spin components to fall in different topological states.

The charge gap for the spin down in Fig. 9(b) closes at Δ_{c2} and the system acquires a finite Chern number. This leads to the z-AFCI. Upon further decreasing of Δ the charge gap for the spin down closes again at Δ_{c1}. The Chern number of the spin-down component vanishes for $\Delta < \Delta_{c1}$ and the system enters a trivial z-AF phase.

Our description of the phase transitions in Fig. 9(b) implies a trivial z-AF phase between the BI and the z-AFCI, although in practice it might be extremely narrow. This is because the magnetic ordering stems from the condensation of an $S = 1$ bound state while the change of the Chern number requires closing of the charge gap. This corresponds to a renormalized staggered potential in Fig. 6(c) being slightly above t rather than being exactly at t at the point where M_z vanishes in Fig. 6(a) and cannot be resolved based on numerical DMFT results. An intervening trivial AF phase between the BI and the AFCI in the case of a continuous transition is also pointed out in Ref. [39] based on bifurcation of a Weyl line due to the

AF ordering. Further research is needed to clarify the emergence of the AFCI based on vanishing of different energy gaps proposed in Fig. 9(b). Using the numerical renormalization group instead of the ED as the impurity solver in DMFT might help to better resolve the behavior of the charge gap across the AFCI. Beyond the DMFT, a method such as the continuous unitary transformations [91–93] which provides a quantitative description of the elementary excitations and their interactions can shine more light on various excitation energies, including both the charge and the spin gap, and the stabilization of the AFCI. The method is already applied to the ionic Hubbard model [66] and can be employed to address also the effect of the finite spin-orbit coupling.

VII. CONCLUSION

In this paper we demonstrate the existence of the collinear AFCI in a square-lattice system which preserves the inversion symmetry. Our analysis relies on a minimal extension of the time-reversal-invariant Harper-Hofstadter-Hubbard (TRI HHH) model which permits to study the competition of the BI, the QSHI, and the Néel AF Mott insulator phases by varying the Hubbard repulsion U and a sublattice potential Δ and examine the existence of the AFCI phase beyond the noncentrosymmetric Kane-Mele-Hubbard model [39].

We map out the phase diagram of the model in the U-Δ plane showing a very close similarity with the phase diagram proposed for the noncentrosymmetric Kane-Mele-Hubbard model [39]. The AFCI appears between the BI and the AF Mott insulator in the limit of large U and Δ. The close similarity of the results obtained for the two very different models suggests that the AFCI is a generic phase which exists beyond a specific model or a lattice structure. We discuss the stabilization of the AFCI based on the vanishing of the charge and the spin gap and emphasize that the necessary condition to realize the AFCI is the lack of a space-group operation to compensate the effect of the time-reversal transformation on the electronic state, which can be achieved on different lattice structures with or without the inversion symmetry.

Optical lattices provide a versatile platform to study the interplay of two-particle interaction and spin-orbit coupling [94]. The correlation strength is highly tunable by using Feshbach resonances or by changing the optical lattice depth, and there has been impressive progress in the past decade in creation of artificial gauge fields using, for example, lattice shaking or laser-assisted tunneling techniques [95]. Fundamental topological models such as the Haldane model [10] and the TRI Harper-Hofstadter model [48,49] have thus been realized. The Chern number of the Hofstadter bands has been measured [96] and the phase diagram of the Haldane model has been mapped out [10]. The high control and tunability of quantum gases in optical lattices would allow to directly investigate our proposed phase diagram in Fig. 2. According to our results, the AFCI can be realized by driving the system from the AF Mott insulator to the BI phase in the limit of large U and Δ.

Since the experimental discovery of the quantum anomalous Hall effect in Cr-doped $(Bi,Sb)_2Te_3$ thin films about a decade ago [11] there has been extensive research to increase the observation temperature of the effect [15,97]. In the current realizations of the CI, the magnetic ordering and the electronic properties stem from electrons in different orbitals [4,5,15,97]. While the strongly interacting electrons in a $3d$ or $4f$ orbital are the origin of the magnetic ordering, the noninteracting electrons in $6p$ and $5p$ orbitals define the electronic properties [24]. The coupling between the magnetic and the electronic degrees of freedom can be seen as an AF Kondo interaction [27]. In contrast, in the AFCI phase we discussed in this paper the electronic and the magnetic properties are inherently coupled as they originate from the same, strongly interacting, electrons. Such a strongly correlated AFCI is expected to show a strong magnetic blueshift of the charge gap upon developing the magnetic order below the Néel temperature [34,35]. This would allow to realize the quantum anomalous Hall effect at temperatures closer to the magnetic transition temperature of the material. Transition metal elements with partially filled $4d$ and $5d$ shells such as iridates [98,99] are potential candidates to observe the combined effect of the strong correlation and the spin-orbit coupling and to realize the AFCI phase.

ACKNOWLEDGMENTS

We would like to thank Y. Xu, A. Dutta, and I. Titvinidze for useful discussions. This work was supported by the Deutsche Forschungsgemeinschaft (DFG, German Research Foundation) via Research Unit FOR 2414 under Project No. 277974659 (M.E. and W.H.). This work was also supported financially in TRR 160 (M.H.-T. and G.S.U.) by the DFG and via the high-performance computing center Center for Scientific Computing (CSC).

[1] M. Z. Hasan and C. L. Kane, Colloquium: Topological insulators, Rev. Mod. Phys. **82**, 3045 (2010).

[2] X.-L. Qi and S.-C. Zhang, Topological insulators and superconductors, Rev. Mod. Phys. **83**, 1057 (2011).

[3] F. D. M. Haldane, Model for a quantum Hall effect without Landau levels: Condensed-matter realization of the "parity anomaly", Phys. Rev. Lett. **61**, 2015 (1988).

[4] C.-X. Liu, S.-C. Zhang, and X.-L. Qi, The quantum anomalous Hall effect: Theory and experiment, Annu. Rev. Condens. Matter Phys. **7**, 301 (2016).

[5] Y. Tokura, K. Yasuda, and A. Tsukazaki, Magnetic topological insulators, Nat. Rev. Phys. **1**, 126 (2019).

[6] C. L. Kane and E. J. Mele, Quantum Spin Hall Effect in Graphene, Phys. Rev. Lett. **95**, 226801 (2005).

[7] B. A. Bernevig and S.-C. Zhang, Quantum Spin Hall Effect, Phys. Rev. Lett. **96**, 106802 (2006).

[8] B. A. Bernevig, T. L. Hughes, and S.-C. Zhang, Quantum spin Hall effect and topological phase transition in HgTe quantum wells, Science **314**, 1757 (2006).

[9] Markus Konig, S. Wiedmann, C. Brüne, A. Roth, H. Buhmann, L. W. Molenkamp, X.-L. Qi, and S.-C. Zhang, Quantum spin Hall insulator state in HgTe quantum wells, Science **318**, 766 (2007).

[10] G. Jotzu, M. Messer, R. Desbuquois, M. Lebrat, T. Uehlinger, D. Greif, and T. Esslinger, Experimental realization of the topological Haldane model with ultracold fermions, Nature (London) **515**, 237 (2014).

[11] C.-Z. Chang, J. Zhang, X. Feng, J. Shen, Z. Zhang, M. Guo, K. Li, Y. Ou, P. Wei, L.-L. Wang, Z.-Q. Ji, Y. Feng, S. Ji, X. Chen, J. Jia, X. Dai, Z. Fang, S.-C. Zhang, K. He, Y. Wang *et al.*, Experimental observation of the quantum anomalous Hall effect in a magnetic topological insulator, Science **340**, 167 (2013).

[12] R. Yu, W. Zhang, H.-J. Zhang, S.-C. Zhang, X. Dai, and Z. Fang, Quantized anomalous Hall effect in magnetic topological insulators, Science **329**, 61 (2010).

[13] X. Kou, L. Pan, J. Wang, Y. Fan, E. S. Choi, W.-L. Lee, T. Nie, K. Murata, Q. Shao, S.-C. Zhang, and K. L. Wang, Metal-to-insulator switching in quantum anomalous Hall states, Nat. Commun. **6**, 8474 (2015).

[14] M. Mogi, R. Yoshimi, A. Tsukazaki, K. Yasuda, Y. Kozuka, K. S. Takahashi, M. Kawasaki, and Y. Tokura, Magnetic modulation doping in topological insulators toward higher-temperature quantum anomalous Hall effect, Appl. Phys. Lett. **107**, 182401 (2015).

[15] P. Wang, J. Ge, J. Li, Y. Liu, Y. Xu, and J. Wang, Intrinsic magnetic topological insulators, The Innovation **2**, 100098 (2021).

[16] J. Li, Y. Li, S. Du, Z. Wang, B.-L. Gu, S.-C. Zhang, K. He, W. Duan, and Y. Xu, Intrinsic magnetic topological insulators in van der Waals layered $MnBi_2$ Te_4-family materials, Sci. Adv. **5**, eaaw5685 (2019).

[17] M. M. Otrokov, I. I. Klimovskikh, H. Bentmann, D. Estyunin, A. Zeugner, Z. S. Aliev, S. Gaß, A. U. B. Wolter, A. V. Koroleva, A. M. Shikin, M. Blanco-Rey, M. Hoffmann, I. P. Rusinov, A. Y. Vyazovskaya, S. V. Eremeev, Y. M. Koroteev, V. M. Kuznetsov, F. Freyse, J. Sánchez-Barriga, I. R. Amiraslanov *et al.*, Prediction and observation of an antiferromagnetic topological insulator, Nature (London) **576**, 416 (2019).

[18] Y. Gong, J. Guo, J. Li, K. Zhu, M. Liao, X. Liu, Q. Zhang, L. Gu, L. Tang, X. Feng, D. Zhang, W. Li, C. Song, L. Wang, P. Yu, X. Chen, Y. Wang, H. Yao, W. Duan, Y. Xu *et al.*, Experimental realization of an intrinsic magnetic topological insulator, Chin. Phys. Lett. **36**, 076801 (2019).

[19] B. Chen, F. Fei, D. Zhang, B. Zhang, W. Liu, S. Zhang, P. Wang, B. Wei, Y. Zhang, Z. Zuo, J. Guo, Q. Liu, Z. Wang, X. Wu, J. Zong, X. Xie, W. Chen, Z. Sun, S. Wang, Y. Zhang *et al.*, Intrinsic magnetic topological insulator phases in the Sb doped $MnBi_2$ Te_4 bulks and thin flakes, Nat. Commun. **10**, 4469 (2019).

[20] J. Wu, F. Liu, M. Sasase, K. Ienaga, Y. Obata, R. Yukawa, K. Horiba, H. Kumigashira, S. Okuma, T. Inoshita, and H. Hosono, Natural van der Waals heterostructural single crystals with both magnetic and topological properties, Sci. Adv. **5** (2019).

[21] C. Hu, K. N. Gordon, P. Liu, J. Liu, X. Zhou, P. Hao, D. Narayan, E. Emmanouilidou, H. Sun, Y. Liu, H. Brawer, A. P. Ramirez, L. Ding, H. Cao, Q. Liu, D. Dessau, and N. Ni, A van der Waals antiferromagnetic topological insulator with weak interlayer magnetic coupling, Nat. Commun. **11**, 97 (2020).

[22] Y.-J. Hao, P. Liu, Y. Feng, X.-M. Ma, E. F. Schwier, M. Arita, S. Kumar, C. Hu, R. Lu, M. Zeng, Y. Wang, Z. Hao, H.-Y. Sun, K. Zhang, J. Mei, N. Ni, L. Wu, K. Shimada, C. Chen, Q. Liu *et al.*, Gapless Surface Dirac Cone in Antiferromagnetic Topological Insulator $MnBi_2$ Te_4, Phys. Rev. X **9**, 041038 (2019).

[23] Y. J. Chen, L. X. Xu, J. H. Li, Y. W. Li, H. Y. Wang, C. F. Zhang, H. Li, Y. Wu, A. J. Liang, C. Chen, S. W. Jung, C. Cacho, Y. H. Mao, S. Liu, M. X. Wang, Y. F. Guo, Y. Xu, Z. K. Liu, L. X. Yang, and Y. L. Chen, Topological Electronic Structure and its Temperature Evolution in Antiferromagnetic Topological Insulator $MnBi_2$ Te_4, Phys. Rev. X **9**, 041040 (2019).

[24] H. Li, S.-Y. Gao, S.-F. Duan, Y.-F. Xu, K.-J. Zhu, S.-J. Tian, J.-C. Gao, W.-H. Fan, Z.-C. Rao, J.-R. Huang, J.-J. Li, D.-Y. Yan, Z.-T. Liu, W.-L. Liu, Y.-B. Huang, Y.-L. Li, Y. Liu, G.-B. Zhang, P. Zhang, T. Kondo *et al.*, Dirac Surface States in Intrinsic Magnetic Topological Insulators $EuSn_2$ As_2 and $MnBi_{2n}$ Te_{3n+1}, Phys. Rev. X **9**, 041039 (2019).

[25] P. Swatek, Y. Wu, L.-L. Wang, K. Lee, B. Schrunk, J. Yan, and A. Kaminski, Gapless Dirac surface states in the antiferromagnetic topological insulator $MnBi_2$ Te_4, Phys. Rev. B **101**, 161109(R) (2020).

[26] Y. Deng, Y. Yu, M. Z. Shi, Z. Guo, Z. Xu, J. Wang, X. H. Chen, and Y. Zhang, Quantum anomalous Hall effect in intrinsic magnetic topological insulator $MnBi_2$ Te_4, Science **367**, 895 (2020).

[27] T. Yoshida, R. Peters, and N. Kawakami, Restoration of topological properties at finite temperatures in a heavy-fermion system, Phys. Rev. B **93**, 045138 (2016).

[28] V. Baltz, A. Manchon, M. Tsoi, T. Moriyama, T. Ono, and Y. Tserkovnyak, Antiferromagnetic spintronics, Rev. Mod. Phys. **90**, 015005 (2018).

[29] J. Diouri, J. P. Lascaray, and M. E. Amrani, Effect of the magnetic order on the optical-absorption edge in Cd_{1-x} Mn_x Te, Phys. Rev. B **31**, 7995 (1985).

[30] C. Ferrer-Roca, A. Segura, C. Reig, and V. Muñoz, Temperature and pressure dependence of the optical absorption in hexagonal MnTe, Phys. Rev. B **61**, 13679 (2000).

[31] G. Sangiovanni, A. Toschi, E. Koch, K. Held, M. Capone, C. Castellani, O. Gunnarsson, S.-K. Mo, J. W. Allen, H.-D. Kim, A. Sekiyama, A. Yamasaki, S. Suga, and P. Metcalf, Static versus dynamical mean-field theory of Mott antiferromagnets, Phys. Rev. B **73**, 205121 (2006).

[32] X. Wang, E. Gull, L. de' Medici, M. Capone, and A. J. Millis, Antiferromagnetism and the gap of a Mott insulator: Results from analytic continuation of the self-energy, Phys. Rev. B **80**, 045101 (2009).

[33] L. Fratino, P. Sémon, M. Charlebois, G. Sordi, and A.-M. S. Tremblay, Signatures of the Mott transition in the antiferromagnetic state of the two-dimensional Hubbard model, Phys. Rev. B **95**, 235109 (2017).

[34] D. Bossini, M. Terschanski, F. Mertens, G. Springholz, A. Bonanni, G. S. Uhrig, and M. Cinchetti, Exchange-mediated magnetic blue-shift of the band-gap energy in the antiferromagnetic semiconductor MnTe, New J. Phys. **22**, 083029 (2020).

[35] M. Hafez-Torbati, D. Bossini, F. B. Anders, and G. S. Uhrig, Magnetic blue shift of Mott gaps enhanced by double exchange, Phys. Rev. Res. **3**, 043232 (2021).

[36] M. Ebrahimkhas, M. Hafez-Torbati, and W. Hofstetter, Lattice symmetry and emergence of antiferromagnetic quantum Hall states, Phys. Rev. B **103**, 155108 (2021).

[37] T. I. Vanhala, T. Siro, L. Liang, M. Troyer, A. Harju, and P. Törmä, Topological Phase Transitions in the Repulsively Interacting Haldane-Hubbard Model, Phys. Rev. Lett. **116**, 225305 (2016).

[38] R. S. K. Mong, A. M. Essin, and J. E. Moore, Antiferromagnetic topological insulators, Phys. Rev. B **81**, 245209 (2010).

[39] K. Jiang, S. Zhou, X. Dai, and Z. Wang, Antiferromagnetic Chern Insulators in Noncentrosymmetric Systems, Phys. Rev. Lett. **120**, 157205 (2018).

[40] P. Zhou, C. Q. Sun, and L. Z. Sun, Two dimensional antiferromagnetic Chern insulator: $NiRuCl_6$, Nano Lett. **16**, 6325 (2016).

[41] P. G. Harper, Single band motion of conduction electrons in a uniform magnetic field, Proc. Phys. Soc., Sect. A **68**, 874 (1955).

[42] D. R. Hofstadter, Energy levels and wave functions of Bloch electrons in rational and irrational magnetic fields, Phys. Rev. B **14**, 2239 (1976).

[43] D. J. Thouless, M. Kohmoto, M. P. Nightingale, and M. den Nijs, Quantized Hall Conductance in a Two-Dimensional Periodic Potential, Phys. Rev. Lett. **49**, 405 (1982).

[44] A. Georges, G. Kotliar, W. Krauth, and M. J. Rozenberg, Dynamical mean-field theory of strongly correlated fermion systems and the limit of infinite dimensions, Rev. Mod. Phys. **68**, 13 (1996).

[45] C. L. Kane and E. J. Mele, Z_2 Topological Order and the Quantum Spin Hall Effect, Phys. Rev. Lett. **95**, 146802 (2005).

[46] N. Goldman, I. Satija, P. Nikolic, A. Bermudez, M. A. Martin-Delgado, M. Lewenstein, and I. B. Spielman, Realistic Time-Reversal Invariant Topological Insulators with Neutral Atoms, Phys. Rev. Lett. **105**, 255302 (2010).

[47] D. Cocks, P. P. Orth, S. Rachel, M. Buchhold, K. Le Hur, and W. Hofstetter, Time-Reversal-Invariant Hofstadter-Hubbard Model with Ultracold Fermions, Phys. Rev. Lett. **109**, 205303 (2012).

[48] M. Aidelsburger, M. Atala, M. Lohse, J. T. Barreiro, B. Paredes, and I. Bloch, Realization of the Hofstadter Hamiltonian with Ultracold Atoms in Optical Lattices, Phys. Rev. Lett. **111**, 185301 (2013).

[49] H. Miyake, G. A. Siviloglou, C. J. Kennedy, W. C. Burton, and W. Ketterle, Realizing the Harper Hamiltonian with Laser-Assisted Tunneling in Optical Lattices, Phys. Rev. Lett. **111**, 185302 (2013).

[50] Y. Hatsugai and M. Kohmoto, Energy spectrum and the quantum Hall effect on the square lattice with next-nearest-neighbor hopping, Phys. Rev. B **42**, 8282 (1990).

[51] Z. Wang and S.-C. Zhang, Simplified Topological Invariants for Interacting Insulators, Phys. Rev. X **2**, 031008 (2012).

[52] Z. Wang and B. Yan, Topological Hamiltonian as an exact tool for topological invariants, J. Phys.: Condens. Matter **25**, 155601 (2013).

[53] M. Takahashi, Half-filled Hubbard model at low temperature, J. Phys. C: Solid State Phys. **10**, 1289 (1977).

[54] N. Nagaosa and J. Takimoto, Theory of neutral-ionic transition in organic crystals. I. Monte Carlo simulation of modified Hubbard model, J. Phys. Soc. Jpn. **55**, 2735 (1986).

[55] S. Rachel and K. Le Hur, Topological insulators and Mott physics from the Hubbard interaction, Phys. Rev. B **82**, 075106 (2010).

[56] J. M. Losada, A. Brataas, and A. Qaiumzadeh, Ultrafast control of spin interactions in honeycomb antiferromagnetic insulators, Phys. Rev. B **100**, 060410(R) (2019).

[57] M. Fabrizio, A. O. Gogolin, and A. A. Nersesyan, From Band Insulator to Mott Insulator in One Dimension, Phys. Rev. Lett. **83**, 2014 (1999).

[58] M. Hafez Torbati, N. A. Drescher, and G. S. Uhrig, Dispersive excitations in one-dimensional ionic Hubbard model, Phys. Rev. B **89**, 245126 (2014).

[59] M. Hafez-Torbati, N. A. Drescher, and G. S. Uhrig, From gapped excitons to gapless triplons in one dimension, Eur. Phys. J. B **88**, 3 (2015).

[60] K. Loida, J.-S. Bernier, R. Citro, E. Orignac, and C. Kollath, Probing the Bond Order Wave Phase Transitions of the Ionic Hubbard Model by Superlattice Modulation Spectroscopy, Phys. Rev. Lett. **119**, 230403 (2017).

[61] A. Garg, H. R. Krishnamurthy, and M. Randeria, Can Correlations Drive a Band Insulator Metallic? Phys. Rev. Lett. **97**, 046403 (2006).

[62] M. Ebrahimkhas, Exact diagonalization study of 2D Hubbard model on honeycomb lattice: Semi-metal to insulator transition, Phys. Lett. A **375**, 3223 (2011).

[63] S. S. Kancharla and E. Dagotto, Correlated Insulated Phase Suggests Bond Order between Band and Mott Insulators in Two Dimensions, Phys. Rev. Lett. **98**, 016402 (2007).

[64] N. Paris, K. Bouadim, F. Hébert, G. G. Batrouni, and R. T. Scalettar, Quantum Monte Carlo Study of an Interaction-Driven Band-Insulator–to–Metal Transition, Phys. Rev. Lett. **98**, 046403 (2007).

[65] K. Byczuk, M. Sekania, W. Hofstetter, and A. P. Kampf, Insulating behavior with spin and charge order in the ionic Hubbard model, Phys. Rev. B **79**, 121103(R) (2009).

[66] M. Hafez-Torbati and G. S. Uhrig, Orientational bond and Néel order in the two-dimensional ionic Hubbard model, Phys. Rev. B **93**, 195128 (2016).

[67] J. C. Budich, B. Trauzettel, and G. Sangiovanni, Fluctuation-driven topological Hund insulators, Phys. Rev. B **87**, 235104 (2013).

[68] A. Amaricci, J. C. Budich, M. Capone, B. Trauzettel, and G. Sangiovanni, First-Order Character and Observable Signatures of Topological Quantum Phase Transitions, Phys. Rev. Lett. **114**, 185701 (2015).

[69] B. Irsigler, J.-H. Zheng, and W. Hofstetter, Interacting Hofstadter Interface, Phys. Rev. Lett. **122**, 010406 (2019).

[70] M. Hafez-Torbati, J.-H. Zheng, B. Irsigler, and W. Hofstetter, Interaction-driven topological phase transitions in fermionic SU(3) systems, Phys. Rev. B **101**, 245159 (2020).

[71] B. Irsigler, J.-H. Zheng, M. Hafez-Torbati, and W. Hofstetter, Spin-imbalance-induced transverse magnetization in the Hofstadter-Hubbard model, Phys. Rev. A **99**, 043628 (2019).

[72] M. Potthoff and W. Nolting, Surface metal-insulator transition in the Hubbard model, Phys. Rev. B **59**, 2549 (1999).

[73] Y. Song, R. Wortis, and W. A. Atkinson, Dynamical mean field study of the two-dimensional disordered Hubbard model, Phys. Rev. B **77**, 054202 (2008).

[74] M. Snoek, I. Titvinidze, C. Tőke, K. Byczuk, and W. Hofstetter, Antiferromagnetic order of strongly interacting fermions in a trap: Real-space dynamical mean-field analysis, New J. Phys. **10**, 093008 (2008).

[75] M. Hafez-Torbati and W. Hofstetter, Artificial SU(3) spin-orbit coupling and exotic Mott insulators, Phys. Rev. B **98**, 245131 (2018).

[76] M. Caffarel and W. Krauth, Exact Diagonalization Approach to Correlated Fermions in Infinite Dimensions: Mott Transition and Superconductivity, Phys. Rev. Lett. **72**, 1545 (1994).

[77] Q. Niu, D. J. Thouless, and Y.-S. Wu, Quantized Hall conductance as a topological invariant, Phys. Rev. B **31**, 3372 (1985).

[78] K. Ishikawa and T. Matsuyama, Magnetic field induced multicomponent QED3 and quantum Hall effect, Z. Phys. C **33**, 41 (1986).

[79] Z. Wang, X.-L. Qi, and S.-C. Zhang, Topological Order Parameters for Interacting Topological Insulators, Phys. Rev. Lett. **105**, 256803 (2010).

[80] V. Gurarie, Single-particle Green's functions and interacting topological insulators, Phys. Rev. B **83**, 085426 (2011).

[81] A. Amaricci, J. C. Budich, M. Capone, B. Trauzettel, and G. Sangiovanni, Strong correlation effects on topological quantum phase transitions in three dimensions, Phys. Rev. B **93**, 235112 (2016).

[82] T. Mertz, K. Zantout, and R. Valentí, Statistical analysis of the Chern number in the interacting Haldane-Hubbard model, Phys. Rev. B **100**, 125111 (2019).

[83] G. Rohringer, H. Hafermann, A. Toschi, A. A. Katanin, A. E. Antipov, M. I. Katsnelson, A. I. Lichtenstein, A. N. Rubtsov, and K. Held, Diagrammatic routes to nonlocal correlations beyond dynamical mean field theory, Rev. Mod. Phys. **90**, 025003 (2018).

[84] C. N. Varney, K. Sun, M. Rigol, and V. Galitski, Interaction effects and quantum phase transitions in topological insulators, Phys. Rev. B **82**, 115125 (2010).

[85] R. Triebl and M. Aichhorn, Topological insulator on honeycomb lattices and ribbons without inversion symmetry, Phys. Rev. B **94**, 165169 (2016).

[86] S. Sachdev and R. N. Bhatt, Bond-operator representation of quantum spins: Mean-field theory of frustrated quantum Heisenberg antiferromagnets, Phys. Rev. B **41**, 9323 (1990).

[87] C. Rüegg, N. Cavadini, A. Furrer, H.-U. Güdel, K. Krämer, H. Mutka, A. Wildes, K. Habicht, and P. Vorderwisch, Bose-Einstein condensation of the triplet states in the magnetic insulator $TlCuCl_3$, Nature (London) **423**, 62 (2003).

[88] C. Rüegg, A. Furrer, D. Sheptyakov, T. Strässle, K. W. Krämer, H.-U. Güdel, and L. Mélési, Pressure-Induced Quantum Phase Transition in the Spin-Liquid $TlCuCl_3$, Phys. Rev. Lett. **93**, 257201 (2004).

[89] T. Nikuni, M. Oshikawa, A. Oosawa, and H. Tanaka, Bose-Einstein Condensation of Dilute Magnons in $TlCuCl_3$, Phys. Rev. Lett. **84**, 5868 (2000).

[90] T. Fischer, S. Duffe, and G. S. Uhrig, Microscopic model for Bose-Einstein condensation and quasiparticle decay, Europhys. Lett. **96**, 47001 (2011).

[91] C. Knetter and G. Uhrig, Perturbation theory by flow equations: Dimerized and frustrated $S = 1/2$ chain, Eur. Phys. J. B **13**, 209 (2000).

[92] H. Krull, N. A. Drescher, and G. S. Uhrig, Enhanced perturbative continuous unitary transformations, Phys. Rev. B **86**, 125113 (2012).

[93] M. Powalski, G. S. Uhrig, and K. P. Schmidt, Roton Minimum as a Fingerprint of Magnon-Higgs Scattering in Ordered Quantum Antiferromagnets, Phys. Rev. Lett. **115**, 207202 (2015).

[94] W. Hofstetter and T. Qin, Quantum simulation of strongly correlated condensed matter systems, J. Phys. B: At., Mol. Opt. Phys. **51**, 082001 (2018).

[95] M. Aidelsburger, S. Nascimbene, and N. Goldman, Artificial gauge fields in materials and engineered systems, C. R. Phys. **19**, 394 (2018).

[96] M. Aidelsburger, M. Lohse, C. Schweizer, M. Atala, J. T. Barreiro, S. Nascimbène, N. R. Cooper, I. Bloch, and N. Goldman, Measuring the Chern number of Hofstadter bands with ultracold bosonic atoms, Nat. Phys. **11**, 162 (2015).

[97] J. Liu and T. Hesjedal, Magnetic topological insulator heterostructures: A review, Adv. Mater. 2102427 (2021).

[98] J. G. Rau, E. K.-H. Lee, and H.-Y. Kee, Spin-orbit physics giving rise to novel phases in correlated systems: Iridates and related materials, Annu. Rev. Condens. Matter Phys. **7**, 195 (2016).

[99] J. Bertinshaw, Y. Kim, G. Khaliullin, and B. Kim, Square lattice iridates, Annu. Rev. Condens. Matter Phys. **10**, 315 (2019).